EuroSun2026

Optical-Thermal Investigation of Cavity Geometry Effects on Flux Redistribution and Thermal Performance of Small-Scale Helical Receivers

Vijay Shanker (corresponding author), Anish Modi

Department of Energy Science and Engineering, Indian Institute of Technology Bombay, Powai, Mumbai 400076, Maharashtra, India

vijay.shanker@iitb.ac.in, anishmodi@iitb.ac.in

Summary

This study investigates the influence of cavity-wall geometry on the optical-thermal performance of small-scale solar central receivers employing a helical absorber configuration. cuboid-cylindrical and cuboid-parabolic cavity geometries are analysed and compared with a previously reported cubical cavity configuration. A three-dimensional numerical model is employed to evaluate solar-flux distribution, thermal losses, thermal efficiency, and heat-flux and temperature uniformity under identical operating conditions. The effect of the non-dimensional pitch (p/d_{o}), varying from approximately 1.65 to 2.57, on the receiver performance is investigated for absorber tube diameters of 76.7 mm and 80.9 mm. The results show that cavity geometry influences the redistribution of incident solar radiation and the resulting thermal performance. The cuboid-cylindrical cavity attains its maximum thermal efficiency at $p/d_{\mathrm{o}} \approx 1.8$, compared with about 2.0 for the cubical and the cuboid-parabolic cavity shapes. Although the cuboid-cylindrical cavity provides improved heat-flux uniformity, its higher thermal losses result in lower thermal efficiency, while the cuboid- parabolic cavity exhibits the highest thermal efficiency among the configurations investigated. Further optical analysis shows that the fraction of the solar power entering the aperture which is ultimately absorbed by the helical absorber, decreases markedly with increasing cavity-wall absorptivity, whereas the differences among the three cavity geometries remain comparatively small. The findings indicate that cavity geometry primarily influences the spatial redistribution of solar energy and the resulting thermal behaviour rather than substantially altering the total solar energy absorbed by the absorber, highlighting the trade-off between flux homogenisation and thermal efficiency in the optimisation of compact solar tower receivers.

Keywords: solar tower, flux uniformity, temperature uniformity, thermal efficiency, solar-radiation absorption, non-dimensional pitch

Field of application for the findings: Small-scale concentrating solar power systems, solar thermal receiver design, cavity receiver optimisation.

Addressed audience: Researchers, thermal engineers, CSP system designers, solar energy researchers, and graduate students working in concentrating solar thermal technologies.

1. Introduction

Decarbonisation of industrial processes requiring high-temperature heat, typically from 150 °C to above 500 °C, remains a major challenge in the transition towards sustainable energy systems. Concentrating solar power (CSP) offers a promising route for supplying renewable process heat, with reported levelized costs of energy between USD 60-100 per MWh (Wu et al., 2025). Small-scale central receiver systems are particularly attractive for decentralised applications because of their potential for compact, dispatchable, and high-temperature thermal-energy generation. Recent studies have demonstrated their applicability to thermal energy storage, industrial process heat, thermochemical fuel production, and integration with small power-generation systems (Liu et al., 2022, 2025; Kadohiro et al., 2025; Giostri et al., 2020). The development of small-scale and modular central receiver concepts has also been pursued through initiatives such as Polyphem and ASTRI (The Polyphem Project, 2025; Asselineau et al., 2019).

The receiver plays a critical role in determining the optical-thermal performance of a central receiver system. In cavity receivers, the absorber converts concentrated solar radiation into thermal energy, while the surrounding cavity influences radiation redistribution and thermal losses. Helical absorbers are attractive in this context because of their compact geometry and favourable heat-transfer characteristics. Sharma et al. (2021), for example, demonstrated the influence of geometric parameters on the thermal performance of a tapered helical-coil cavity receiver. More recently, Shanker and Modi (2026) investigated a helical absorber centrally positioned within a cubical cavity and found that maximum thermal efficiency occurred at a non-dimensional pitch $p/d_\mathrm{o} \approx 2$, rather than for the most tightly coiled configuration. This behaviour indicated an important contribution from solar radiation reaching the rear cavity wall and subsequently being redistributed towards the absorber.

This observation suggests that cavity-wall geometry itself may influence the optical-thermal behaviour of a helical receiver. Previous investigations of other cavity-receiver configurations have shown that cavity geometry can modify internal radiative redistribution, optical efficiency, and surface heat-flux distribution. For example, Wang et al. (2016) demonstrated that internal radiative redistribution can reduce reflection losses and improve the distribution of concentrated solar energy, while Daabo et al. (2016) reported substantial differences in optical performance among cylindrical, conical, and spherical cavity geometries. Such redistribution is also important because non-uniform heat flux can produce localised temperature gradients and thermal stresses. Previous numerical and experimental studies have shown that receiver geometry and flux redistribution can considerably affect both heat-flux and temperature uniformity (Qiu et al., 2017; Najafabadi and Ozalp, 2018).

Despite these developments, the influence of cavity-wall geometry on the coupled optical and thermal performance of small-scale helical cavity receivers remains insufficiently investigated, particularly with respect to heat-flux redistribution, flux and temperature uniformity, thermal losses, and thermal efficiency. Building upon the cubical cavity receiver investigated by Shanker and Modi (2026), the present study therefore compares the cubical configuration with two modified geometries: a semi-cylindrical cuboidal cavity, hereafter termed the *cuboid-cylindrical cavity*, and a parabolic cuboidal cavity, hereafter termed the *cuboid-parabolic cavity*. A three-dimensional optical–thermal model is employed to examine the influence of cavity geometry and non-dimensional absorber pitch on radiative redistribution, heat-flux and temperature uniformity, thermal losses, and thermal efficiency. The study thereby aims to assess the performance of various cavity geometries in the design and optimisation of compact helical receivers for small-scale CSP applications.

2. Methodology

2.1 Receiver Configuration

The proposed receiver consists of a helical absorber as shown in Fig. 1a, enclosed within cubical cavity receiver shown in Fig. 1b and two modified cavity geometries, namely a cuboid-cylindrical cavity and a cuboid-parabolic cavity, as shown in Fig. 1c and Fig. 1d respectively. The cavity enclosure is intended to reduce convective and radiative heat losses, while the modified cavity wall geometries are investigated to assess their influence on radiative redistribution, heat-flux distribution, and overall receiver performance. The receiver is designed for a small-scale thermal power output of 1 MW and receives concentrated solar radiation from a polar-oriented heliostat field.

To enable a direct comparison with the cubical cavity investigated in our previous study (Shanker and Modi, 2026), all operating conditions and geometric parameters were retained, with the cavity wall geometry being the only modification introduced in the present work. The non-dimensional pitch (p/d_o) is selected as the primary design parameter because it provides a direct measure of the compactness of the helical absorber coil. A non-dimensional pitch close to unity corresponds to a fully compressed configuration in which successive turns of the absorber are in contact with negligible spacing between them. As the pitch increases, larger portions of the absorber surface and cavity wall become exposed to the incident solar radiation. Since the cavity wall possesses a lower absorptivity than the absorber surface, a greater fraction of the incident radiation striking these exposed wall regions is reflected and subsequently reabsorbed by other portions of the helical absorber. Consequently, the cavity wall geometry is expected to play an important role in determining the extent of radiative redistribution and the resulting thermal performance of the receiver.

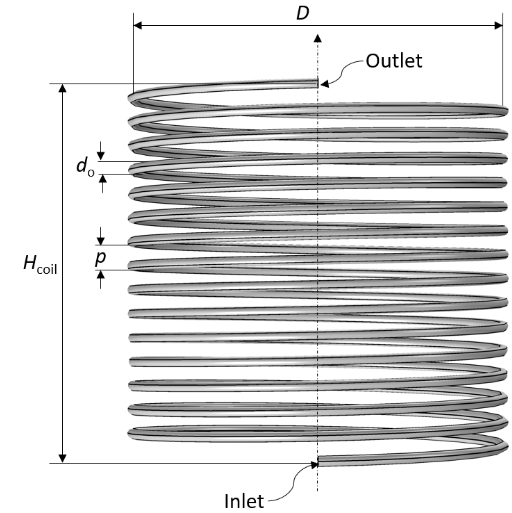

(a) Helical absorber

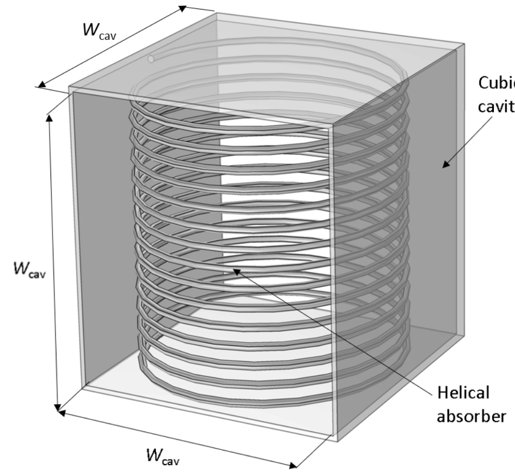

(b) Cubical cavity receiver

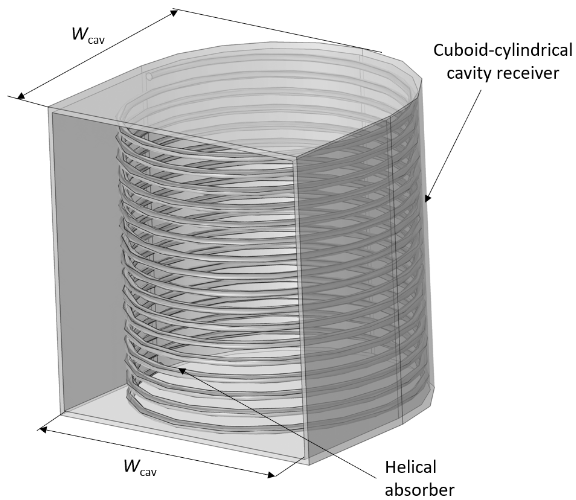

(c) Cuboid-cylindrical cavity receiver

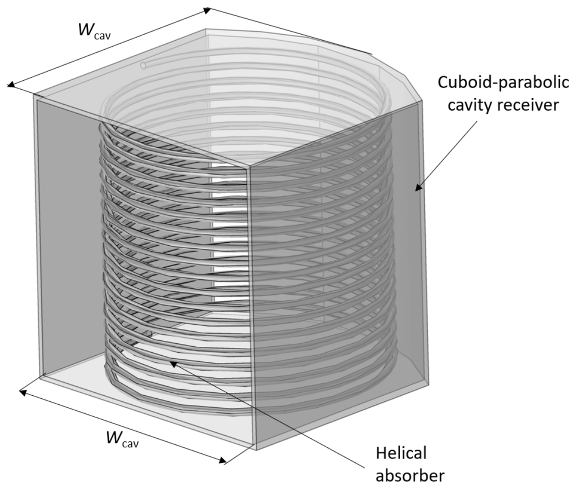

(d) Cuboid-parabolic cavity receiver

Fig. 1: Schematic diagrams of (a) the helical absorber and the corresponding (b) Cubical, (c) Cuboid-cylindrical, and (d) Cuboid- parabolic cavity receiver configurations. Here, D, d_o, p, and H_{coil} are the helix diameter, absorber-tube outer diameter, helical pitch, and absorber height, respectively, while W_{cav} is the cavity width.

2.2 Optical-Thermal Modelling

The receiver performance is investigated for non-dimensional pitch values ranging from 1.65 to 2.57, representing a transition from a relatively tightly coiled absorber to progressively more widely spaced helical turns. As p/d_o increases, the greater spacing between successive turns exposes a larger portion of the internal cavity walls to the incident solar radiation, thereby increasing the interaction of radiation with the cavity surfaces. The absorber tube diameters of 76.7 mm and 80.9 mm were considered. The cuboid-cylindrical cavity comprises a semi-cylindrical rear section and a cuboidal front section, as shown in Fig. 1c, with the cylindrical wall arranged coaxially with the helical absorber. The cuboid-parabolic cavity incorporates a parabolic rear wall whose focal axis coincides with the axis of the helical absorber, as shown in Figure 3b. For consistency with the reference cubical cavity configuration, all cavity geometries considered in the present study have the same square aperture and cavity depth. For the cuboid-cylindrical and cuboid-parabolic cavities, the specified cavity depth refers to the maximum depth measured from the cavity aperture plane.

The schematic representation of the heliostat field and receiver employed in the simulations is shown in Fig. 2.

The optical-thermal modelling methodology follows the validated approach reported by Shanker and Modi (2026). Initially, the heliostat field is modelled using SolarPILOT version 1.5.2 (Wagner and Wendelin, 2018) for a target receiver thermal power of 1 MW, using preliminary estimates of the receiver optical and thermal losses. The resulting heliostat-field configuration is subsequently imported into COMSOL Multiphysics version 6.0 (COMSOL AB, 2022) for optical and thermal analyses. Ray-tracing simulations are performed in COMSOL to determine the spatial distribution of concentrated solar radiation incident on the receiver and the resulting non-uniform heat-flux distribution over the absorber surface. The corresponding optical and thermal losses evaluated in COMSOL are then incorporated into SolarPILOT, and the heliostat field is re-optimised. This iterative exchange between SolarPILOT and COMSOL is continued until the optimised heliostat-field configuration is obtained. The optimised heliostat field, together with the proposed receiver geometry, is subsequently analysed in COMSOL. The non-uniform heat-flux distribution obtained from the optical analysis is applied as a boundary condition in the thermal model to evaluate the thermal performance of the receiver.

The thermal model solves the steady-state energy equation accounting for solar energy absorption, radiative heat losses, natural convective heat losses, and heat transfer to the molten-salt heat transfer fluid flowing through the absorber tube. All receiver surfaces are assumed to be opaque, grey, and diffuse. Additional details regarding the governing equations, assumptions, boundary conditions, and numerical implementation are available in Shanker and Modi (2026).

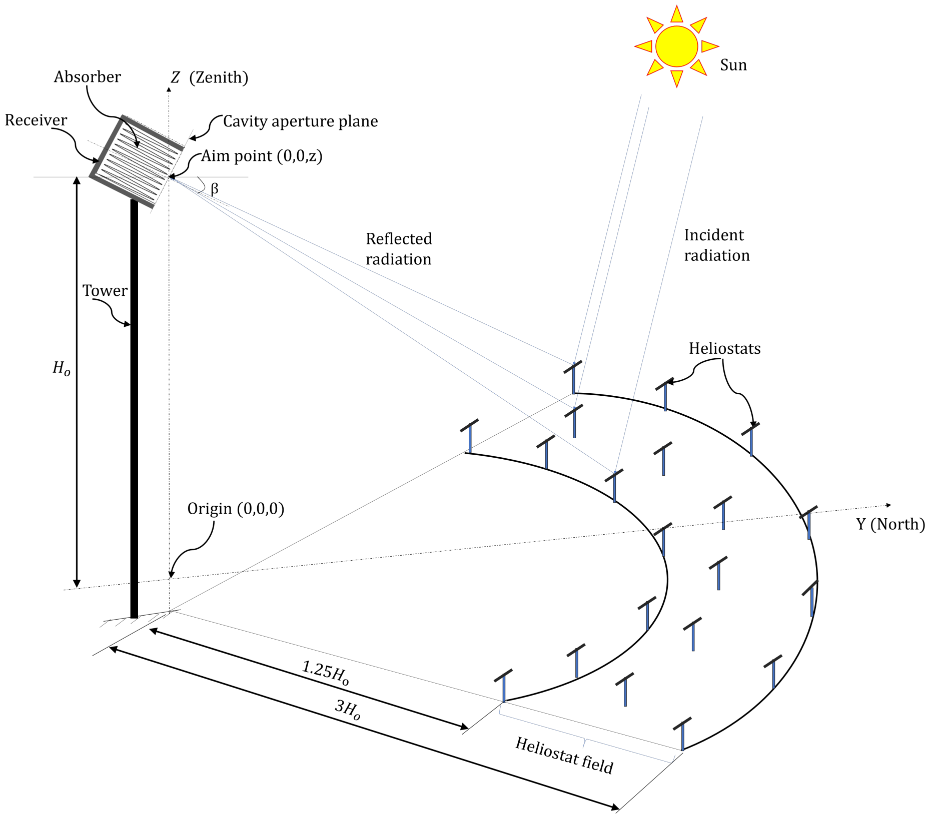

Fig. 2: Schematic of the heliostat field layout showing the receiver tilted at an angle β and the aim point located at $(0, 0, z)$ (Shanker and Modi, 2026).

2.3 Performance parameters

The optical and thermal performance of the proposed cuboid- cavity receivers are subsequently compared with the cubical cavity configuration reported in (Shanker and Modi, 2026). The optical efficiency was calculated using Equation (1).

$$\eta_{\text{opt}} = \frac{\dot{Q}_{\text{coil}} + \dot{Q}_{\text{cav}}}{\text{DNI} \cdot N_{\text{hel}} \cdot A_{\text{hel}}} \tag{1}$$

where $\dot{Q}_{\text{coil}}$ represents the solar power incident on the absorber tube and $\dot{Q}_{\text{cav}}$ denotes the solar power incident on the cavity walls. N_{hel} and A_{hel} denote the number of heliostats and area of the reflecting surface of each heliostat.

The cubical cavity configuration is assessed in the present study using a flux-uniformity metric to facilitate a comparative evaluation of the influence of cavity wall geometry on radiative redistribution. Similar approaches for quantifying flux uniformity have been reported by Daabo et al. (2016). In the present work, the uniformity of the absorber surface heat-flux distribution is quantified using the flux uniformity factor (UF_F), defined as:

$$\text{UF}_\text{F} = 1 - \frac{\sigma_{\dot{q}}}{\dot{q}_{\text{mean}}} \tag{2}$$

where $\dot{q}_{\text{mean}}$ and $\sigma_{\dot{q}}$ denote the area-averaged heat flux and the standard deviation of the absorber surface heat-flux distribution, respectively. These quantities are calculated as follows:

$$\dot{q}_{\text{mean}} = \frac{1}{A}\int_A \dot{q}\, dA \tag{3}$$

$$\sigma_{\dot{q}} = \sqrt{\frac{1}{A}\int_A (\dot{q} - \dot{q}_{\text{mean}})^2\, dA} \tag{4}$$

where A denotes the total absorber surface area. A value of UF_F approaching unity indicates an increasingly uniform heat flux distribution, whereas lower values correspond to greater flux non-uniformity.

To quantify the degree of temperature homogenisation over the absorber surface, a temperature uniformity factor (UF_T) is introduced based on the normalised standard deviation of the surface temperature distribution. Similar temperature-uniformity indices have been employed in studies aimed at mitigating thermal non-uniformity and hot spots in solar receivers by Najafabadi and Ozalp (2018). The temperature uniformity factor is defined as:

$$\text{UF}_\text{T} = 1 - \frac{\sigma_T}{T_{\text{mean}}} \tag{5}$$

where T_{mean} is the area-averaged absorber surface temperature and σ_T is the standard deviation of the absorber surface temperature distribution. These quantities are calculated as follows:

$$T_{\text{mean}} = \frac{1}{A}\int_A T\, dA \tag{6}$$

$$\sigma_T = \sqrt{\frac{1}{A}\int_A (T - T_{\text{mean}})^2\, dA} \tag{7}$$

A value of UF_T approaching unity indicates a highly uniform temperature distribution, whereas lower values correspond to increasing temperature non-uniformity.

Thermal performance is evaluated using the instantaneous thermal efficiency relation given in Equation (8).

$$\eta_{\text{th}} = \frac{\dot{Q}_\text{u}}{\dot{Q}_{\text{coil}} + \dot{Q}_{\text{cav}}} \tag{8}$$

where $\dot{Q}_\text{u}$, $\dot{Q}_{\text{coil}}$, and $\dot{Q}_{\text{cav}}$ represent the useful thermal power and the solar power incident on the absorber tube and cavity walls, respectively.

3. Model Validation

The thermal and hydraulic models were validated using the cuboid- cylindrical cavity receiver by comparing the predicted Nusselt number and Darcy friction factor with the correlations of Seban and McLaughlin (1963) and Mishra and Gupta (1979), respectively. The Seban-McLaughlin correlation is given by:

$$\mathrm{Nu} = 0.023\,\mathrm{Re}^{0.85}\,\mathrm{Pr}^{0.4}\left(1 + 3.5\frac{d_\mathrm{i}}{D}\right) \tag{9}$$

while the Mishra-Gupta correlation is expressed as

$$f = \left[\frac{0.3164}{\mathrm{Re}^{0.25}} + 0.03\left(\frac{d_\mathrm{i}}{D}\right)^{0.5}\right]\left(\frac{\mu_\mathrm{w}}{\mu_\mathrm{f}}\right)^{0.27}, \tag{10}$$

Here, Nu is the Nusselt number, f is the Darcy friction factor, Re and Pr are the Reynolds and Prandtl numbers, respectively, d_i is the inner diameter of the absorber tube, D is the helix diameter, and μ_w and μ_f are the dynamic viscosities of the heat-transfer fluid evaluated at the tube-wall and bulk-fluid temperatures, respectively.

Over the investigated range of $1.64 \le p/d_\mathrm{o} \le 2.57$, the predicted Nusselt numbers differed from the Seban-McLaughlin correlation by 3.34-3.79%, while the friction factors differed from the Mishra-Gupta correlation by 10.1-10.9%. This validated model was subsequently applied to the different cavity geometries investigated in the present study.

4. Results and Discussion

The variation of thermal efficiency with non-dimensional pitch is presented in Fig. 3. For cuboid-cylindrical and cuboid-parabolic cavity geometries, smaller absorber tube diameters result in higher thermal efficiencies over the entire range of non-dimensional pitches investigated. In the case of the cuboid- cylindrical cavity receiver, the thermal efficiency increases with non-dimensional pitch up to an optimum value of approximately 1.8, beyond which it decreases. In contrast, for the cuboid-parabolic cavity receiver, the thermal efficiency reaches a maximum at a non-dimensional pitch of 2.0, as shown in Fig. 3b, and subsequently declines with further increase in pitch.

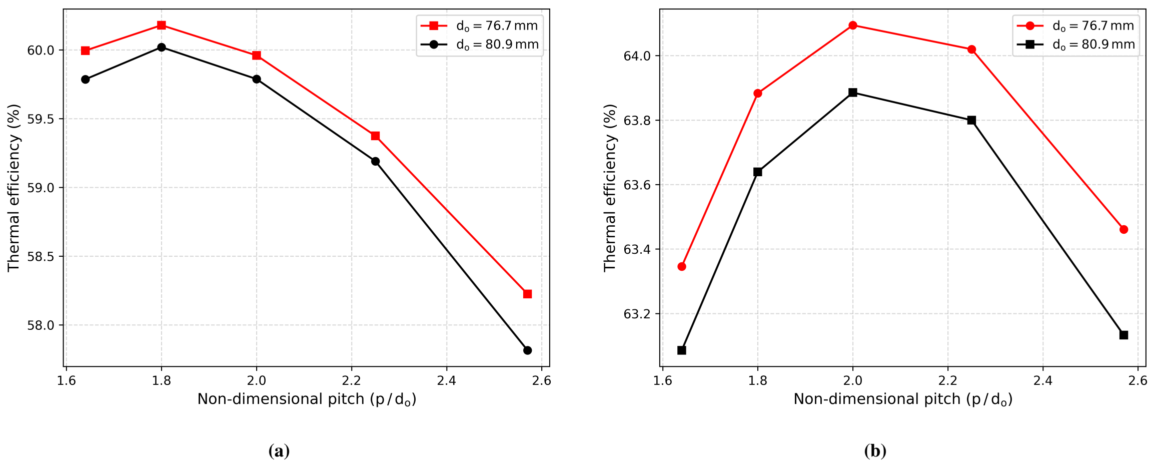

Fig. 3: Effect of non-dimensional pitch on the thermal efficiency of the (a) Cuboid-cylindrical cavity receiver and (b) Cuboid-parabolic cavity receiver for different absorber tube diameters (d_o).

This behaviour can be attributed to the trade-off between optical and thermal losses, which gives rise to an optimum non-dimensional pitch. For the cuboid-cylindrical cavity receiver, this optimum occurs at a non-dimensional pitch of 1.8, whereas for the cuboid-parabolic cavity receiver, it shifts to 2.0. The latter is consistent with the optimum value reported by Shanker and Modi (2026) for a cubical cavity receiver.

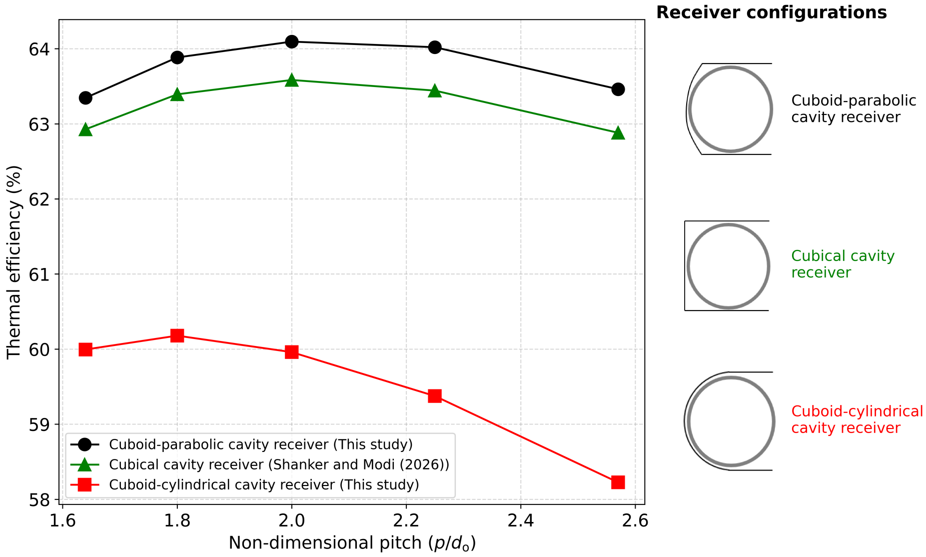

Fig. 4: Comparison of thermal efficiency as a function of non-dimensional pitch (p/d_o) for the cuboid-cylindrical and cuboid-parabolic cavity receivers investigated in the present study and the cubical cavity receiver reported by Shanker and Modi (2026), at an absorber tube outer diameter of d_o = 76.7 mm and an inlet Reynolds number of Re = 22452. The corresponding receiver configurations are illustrated by the top-view schematics on the right. All three cavity geometries have the same square aperture and cavity depth. For the cuboid-cylindrical and cuboid-parabolic cavities, the cavity depth refers to the maximum depth. All depths are measured from the cavity aperture plane, represented by the open side of each schematic.

However, comparison of the thermal efficiencies of the three cavity geometries reveals that the cuboid-parabolic cavity receiver consistently achieves the highest thermal efficiency, followed by the cubical cavity receiver, whereas the cuboid-cylindrical cavity receiver exhibits the lowest thermal efficiency over the entire range of non-dimensional pitches investigated, as shown in Fig. 4. This behaviour can be attributed primarily to the influence of cavity geometry on the interception and redistribution of the incident solar radiation within the receiver. To qualitatively examine the influence of cavity-wall geometry on the spatial variation of absorber-surface heat flux and temperature, representative distributions for the three cavity geometries are compared in Fig. 5. The comparison is performed at p/d_o = 2.0, d_o = 76.7 mm, and Re = 22452, with identical operating conditions for all three configurations, thereby providing a consistent basis for assessing the influence of cavity geometry. At p/d_o = 2.0 and d_o = 76.7 mm, the cuboid-parabolic cavity exhibited the highest heat-flux uniformity, with UF_F = −0.684, compared with −0.700 for the cubical cavity and −0.703 for the cuboid-cylindrical cavity.

In contrast, the temperature uniformity factors were relatively close for the three cavity geometries, with UF_T = 0.898, 0.899, and 0.900 for the cuboid-parabolic, cubical, and cuboid-cylindrical cavities, respectively. Thus, although the cuboid-parabolic cavity provided a more uniform absorber-surface heat-flux distribution, this ordering was not retained for the surface-temperature distribution, for which the cuboid-cylindrical cavity exhibited the highest uniformity. As evident from Fig. 5(a–c), the absorber-surface heat flux is spatially non-uniform for all three cavity geometries, with distinct regions of relatively high and low heat flux. However, the spatial extent and distribution of these regions differ among the cubical, cuboid-cylindrical, and cuboid-parabolic cavities, indicating that the cavity-wall geometry influences the distribution of solar radiation over the absorber surface. The corresponding temperature distributions in Fig. 5(d–f) also exhibit spatial non-uniformity. The temperature patterns do not necessarily reproduce the heat-flux distributions directly. The upper portions of the absorber surfaces exhibit higher temperatures than the lower portions. This temperature variation is primarily attributed to the progressive heating of the working fluid along the flow direction. The cold fluid enters the absorber tubes at the lower end and absorbs heat as it flows upward through the helical absorber. As a result, the fluid temperature increases progressively along the flow path, leading to a reduction in the local temperature difference between the absorber wall and the working fluid. Consequently, the absorber surface temperature increases towards the outlet, resulting in higher temperatures in the upper portions of the absorber.

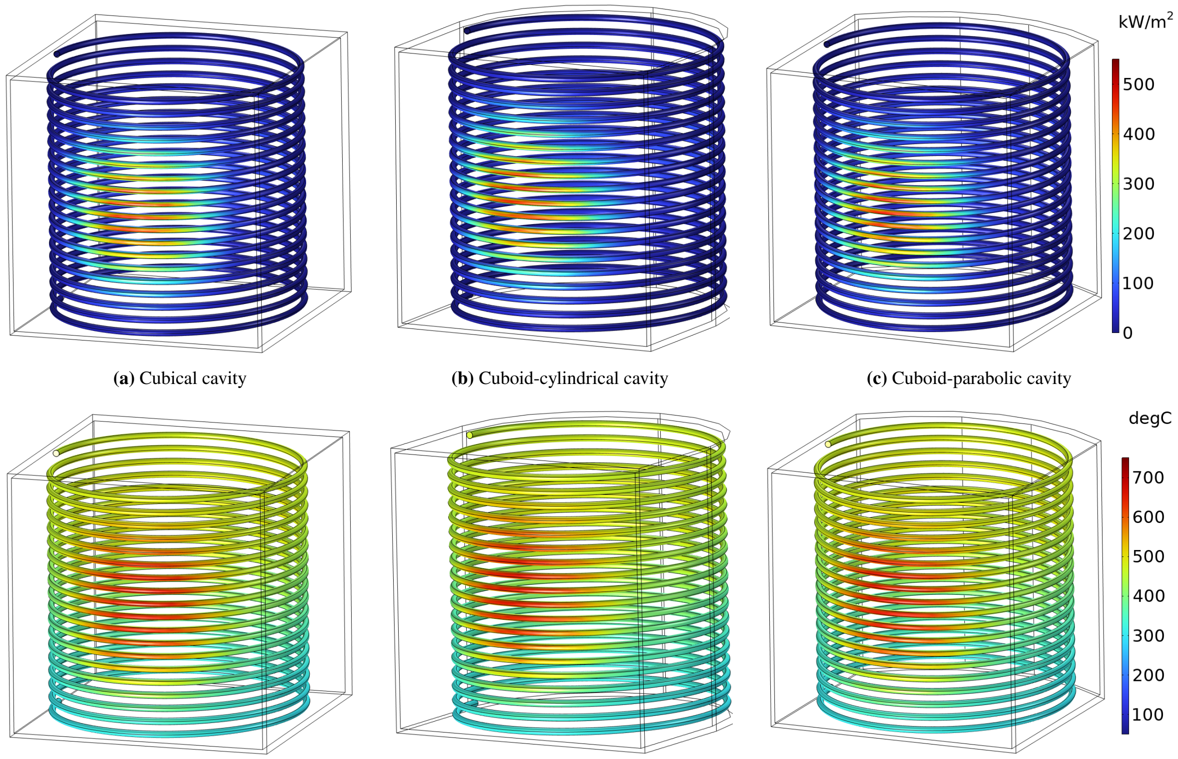

(a) Cubical cavity **(b)** Cuboid-cylindrical cavity **(c)** Cuboid-parabolic cavity

(d) Cubical cavity **(e)** Cuboid-cylindrical cavity **(f)** Cuboid-parabolic cavity

Fig. 5: Comparison of absorber-surface distributions for the single-absorber configuration in the cubical, cuboid-cylindrical, and cuboid-parabolic cavity receivers at p/d_o = 2.0, d_o = 76.7 mm, and an inlet Reynolds number of Re = 22452: (a)-(c) heat-flux distributions and (d)-(f) surface-temperature distributions. Identical colour scales are used within each row to facilitate direct comparison among the cavity geometries. The colour legends shown in (c) and (f) apply to the heat-flux distributions in (a)-(c) and the surface-temperature distributions in (d)-(f), respectively. In the temperature colour legend, `degC` denotes degrees Celsius (°C).

Although these contour distributions provide a qualitative representation of the spatial non-uniformity, visual comparison alone is insufficient to quantify the relative uniformity of the three receiver configurations. Therefore, the heat-flux and temperature distributions are subsequently evaluated using the heat-flux uniformity factor (UF_F) and temperature uniformity factor (UF_T), respectively. Both UF_F and UF_T exhibit an increasing trend with increasing non-dimensional pitch for all the investigated cavity geometries, as shown in Fig. 6a and Fig. 6b, respectively. This behaviour indicates improved redistribution of the incident solar radiation over the absorber surface as the spacing between adjacent helical turns increases. At lower non-dimensional pitch values, the close proximity of neighbouring turns results in substantial inter-turn shadowing and localised flux concentration, thereby reducing the influence of cavity-wall geometry on the overall radiative behaviour. As the non-dimensional pitch increases, the reduced blockage by the absorber tubes exposes a larger portion of the cavity wall to the incident radiation. Consequently, the contribution of cavity-wall reflections and radiative redistribution becomes increasingly significant, resulting in improved heat-flux uniformity.

Among the investigated configurations, the cuboid-parabolic cavity exhibits the highest heat-flux uniformity over nearly the entire range of non-dimensional pitch values considered, as shown in Fig. 6a. An exception is observed at lower non-dimensional pitch values, where the heat-flux uniformity factors of all three cavity geometries are nearly identical. At these lower non-dimensional pitch values, the absorber turns are closely spaced, resulting in significant inter-turn blockage that limits the exposure of the cavity walls to the incident solar radiation. Consequently, the contribution of cavity-wall reflections to radiative redistribution becomes negligible, thereby diminishing the influence of cavity geometry on the heat-flux uniformity. The improved heat-flux uniformity exhibited by the cuboid- parabolic cavity receiver at higher non-dimensional pitches is attributed to the superior radiative redistribution provided by its parabolic cavity surfaces. Unlike the cylindrical and flat cavity walls, the parabolic surfaces redirect a larger fraction of the reflected radiation towards the absorber through multiple internal reflections, thereby producing a more homogeneous heat-flux distribution over the absorber surface.

In contrast, the cuboid-cylindrical cavity exhibits a slightly higher temperature uniformity factor than the other two configurations over the investigated range, as shown in Fig. 6b. This observation indicates that improved heat-flux uniformity does not necessarily translate directly into improved temperature uniformity, since the latter is also influenced by the coupled thermal and fluid-flow characteristics of the absorber.

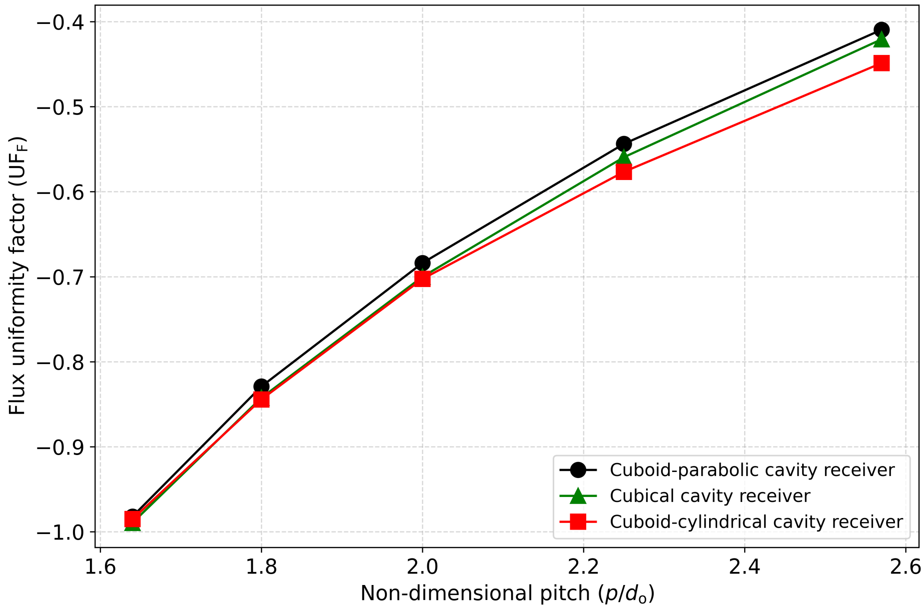

(a)

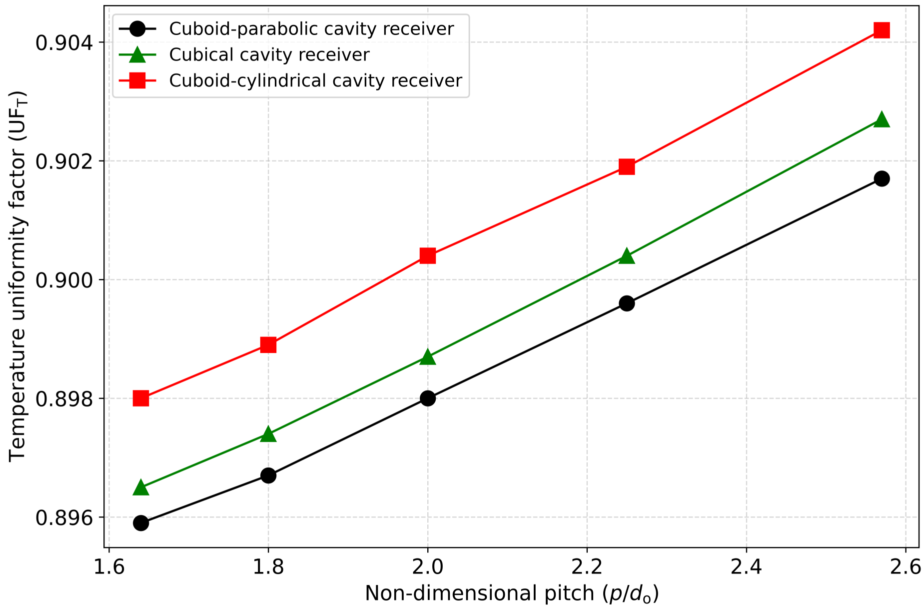

(b)

Fig. 6: Comparison of flux and temperature uniformity factors for different cavity geometries at an absorber tube outer diameter of d_o = 76.7 mm: (a) flux uniformity factor and (b) temperature uniformity factor.

4.1 Effect of Cavity Geometry on Solar-Radiation Absorption

To further examine the influence of cavity geometry on optical performance, the fraction of aperture-entering solar radiation ultimately absorbed by the helical absorber was evaluated as:

$$f_{abs} = \frac{\dot{Q}_{abs}}{\dot{Q}_{ap}}, \tag{11}$$

where $\dot{Q}_{abs}$ is the total solar power absorbed by the helical absorber, including both the solar radiation directly intercepted by the absorber after entering the cavity aperture and the radiation subsequently reflected from the cavity walls and absorbed by the absorber. $\dot{Q}_{ap}$ is the solar power entering the cavity aperture. The analysis was performed at $p/d_o = 2.53$ and $d_o = 76.7$ mm. The relatively large pitch provides greater spacing between successive turns, increasing the interaction of incident radiation with the internal cavity surfaces and thereby facilitating assessment of the effect of cavity geometry.

The solar power entering the aperture, $\dot{Q}_{ap}$, was determined from a separate ray-tracing calculation by setting the solar absorptivity of the absorber and cavity walls to unity. The resulting values were 1678.41, 1677.11, and 1677.88 kW for the cubical, cuboid-cylindrical, and cuboid-parabolic cavities, respectively. The variation was less than 0.1%, confirming that essentially the same solar power entered the aperture for all three configurations. Fig. 7 shows that f_{abs} decreased markedly with increasing cavity wall absorptivity, from approximately 0.86-0.87 at $\alpha_{cav} = 0$ to approximately 0.52 at $\alpha_{cav} = 1$. Increasing wall absorptivity reduces wall reflectance and, consequently, the radiation available for subsequent reflection towards and absorption by the helical absorber. In contrast, only small differences in f_{abs} were observed among the three cavity geometries. This indicates that cavity-wall absorptivity has a stronger influence on the total solar energy absorbed by the absorber, whereas cavity geometry primarily affects its spatial redistribution, as also reflected in the differences in absorber heat flux distribution and uniformity.

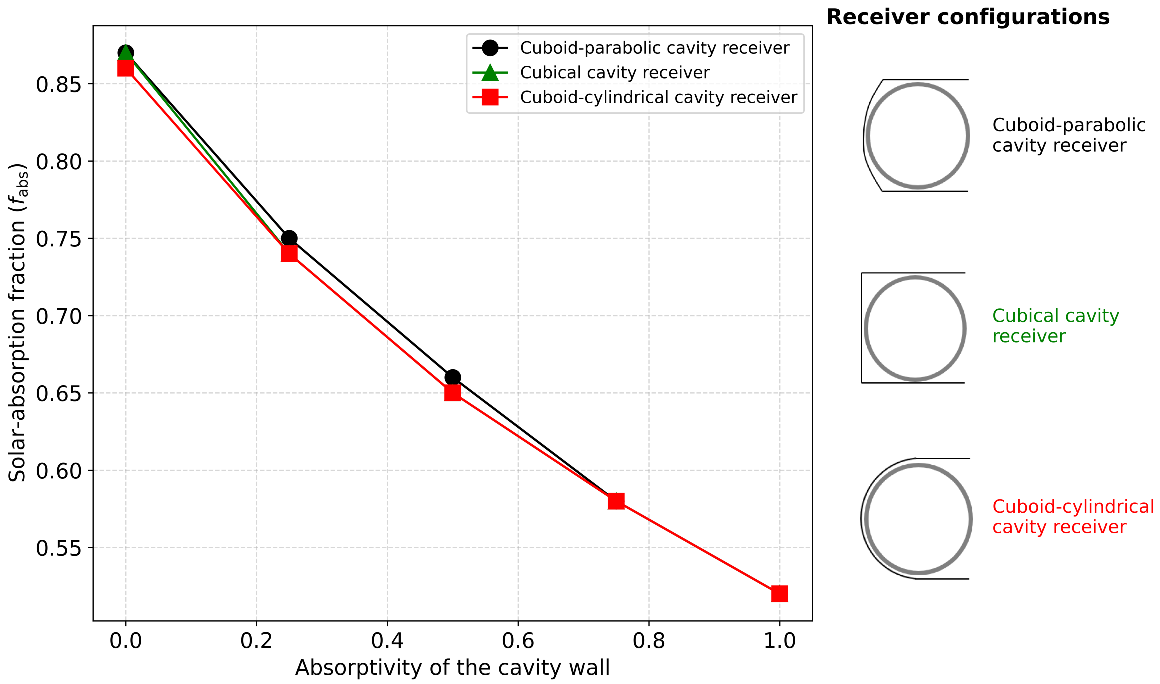

Fig. 7: Variation of the absorber solar-absorption fraction with cavity-wall absorptivity for the different cavity geometries at $p/d_o = 2.53$ and $d_o = 76.7$ mm.

5. Conclusion

The influence of cavity-wall geometry on the optical and thermal performance of a small-scale helical cavity receiver was investigated by comparing cubical, cuboid-cylindrical, and cuboid-parabolic configurations. Cavity geometry was found to influence the spatial distribution of solar radiation over the absorber and the resulting thermal performance. Among the configurations investigated, the cuboid-parabolic cavity exhibited the most favourable overall performance and the highest thermal efficiency, with its optimum occurring at approximately $p/d_o = 2.0$.

The solar-absorption analysis showed that the aperture-entering solar power remained essentially unchanged among the three geometries. Although the absorber solar-absorption fraction decreased markedly with increasing cavity wall absorptivity, only small differences were observed among the cavity geometries. This indicates that cavity wall absorptivity has a stronger influence on the total solar energy absorbed by the absorber, whereas cavity geometry primarily influences its spatial redistribution and the resulting thermal behaviour. Overall, the cuboid-parabolic cavity provides a favourable configuration for improving the performance of small-scale helical central receivers.

6. References

C. A. Asselineau, F. Venn, W. Logie, D. Potter, J. S. Kim, J. Pye, and J. Coventry. Design of astri's high-temperature liquid sodium receiver prototype. *Proceedings of SolarPACES2019*, 2019.

COMSOL AB. *COMSOL Multiphysics® v6.0*. COMSOL AB, Stockholm, Sweden, 2022.

A. M. Daabo, S. Mahmoud, and R. K. Al-Dadah. The effect of receiver geometry on the optical performance of a small-scale solar cavity receiver for parabolic dish applications. *Energy*, 114:513–525, 2016.

A. Giostri, M. Binotti, C. Sterpos, and G. Lozza. Small scale solar tower coupled with micro gas turbine. *Renewable Energy*, 147:570–583, 2020.

Y. Kadohiro, T. Roeder, K. Risthaus, D. Laaber, N. Monnerie, and C. Sattler. Experimental demonstration and validation of tubular solar cavity receivers for simultaneous generation of superheated steam and hot air. *Applied Energy*, 380:125042, 2025.

H. Liu, W. Shuai, Z. Yao, J. Xuan, M. Ni, G. Xiao, and H. Xu. Optimization of solid oxide electrolysis cells using concentrated solar-thermal energy storage: A cuboid- deep learning approach. *Applied Energy*, 377: 124610, 2025.

T. Liu, J. Yang, Z. Yang, and Y. Duan. Techno-economic feasibility of solar power plants considering pv/csp with electrical/thermal energy storage system. *Energy Conversion and Management*, 255:115308, 2022.

P. Mishra and S. N. Gupta. Momentum transfer in curved pipes. 1. newtonian fluids. *Industrial & Engineering Chemistry Process Design and Development*, 18(1):130–137, 1979.

H. A. Najafabadi and N. Ozalp. An advanced modeling and experimental study to improve temperature uniformity of a solar receiver. *Energy*, 165:984–998, 2018.

Y. Qiu, M. Li, K. Wang, Z. Liu, and X. Xue. Aiming strategy optimization for uniform flux distribution in the receiver of a linear fresnel solar reflector using a multi-objective genetic algorithm. *Applied Energy*, 205: 1394–1407, 2017.

R. A. Seban and E. F. McLaughlin. Heat transfer in tube coils with laminar and turbulent flow. *International Journal of Heat and Mass Transfer*, 6(5):387–395, 1963.

V. Shanker and A. Modi. Proposal and performance analysis of a central receiver with helical absorber for small-scale concentrating solar thermal applications. *Results in Engineering*, 30:110297, 2026.

S. Sharma, A. Sah, C. Subramaniam, and S.K. Saha. Performance enhancement of tapered helical coil receiver using novel nanostructured carbon florets coating. *Applied Thermal Engineering*, 194:117065, 2021.

The Polyphem Project. The polyphem project, 2025. URL `https://www.polyphem-project.eu/`. Accessed: 2025-03-07.

M. J. Wagner and T. Wendelin. Solarpilot: A power tower solar field layout and characterization tool. *Solar Energy*, 171:185–196, 2018.

K. Wang, Y. L. He, Y. Qiu, and Y. Zhang. A novel integrated simulation approach couples mcrt and gebhart methods to simulate solar radiation transfer in a solar power tower system with a cavity receiver. *Renewable Energy*, 89:93–107, 2016.

C. Wu, Y. Zhao, W. Li, J. Fan, H. Xu, Z. Ling, D. Yuan, and X. Zeng. Concentrated solar thermal power technology and its thermal applications. *Energies*, 18, 2025.

Appendix: UNITS AND SYMBOLS

Nomenclature and Symbols

The symbols used in the optical-performance analysis and in the quantification of absorber-surface heat-flux and temperature uniformity are summarized below. Dimensionless quantities are indicated by "–" in the unit column.

Table 1: Optical Performance Quantities

Quantity	Symbol	Unit
Optical efficiency	η_{opt}	–
Direct normal irradiance	DNI	$\mathrm{W\,m^{-2}}$
Solar power entering cavity aperture	$\dot{Q}_{\mathrm{ap}}$	W
Solar power incident on absorber tube	$\dot{Q}_{\mathrm{coil}}$	W
Solar power absorbed by absorber tube	$\dot{Q}_{\mathrm{abs}}$	W
Solar power incident on cavity walls	$\dot{Q}_{\mathrm{cav}}$	W
Absorber solar-absorption fraction	f_{abs}	–
Cavity-wall solar absorptivity	α_{cav}	–
Number of heliostats	N_{hel}	–
Reflecting area of each heliostat	A_{hel}	$\mathrm{m^2}$

Table 2: Absorber-Surface Uniformity Quantities

Quantity	Symbol	Unit
Heat-flux uniformity factor	$\mathrm{UF_F}$	–
Local absorber surface heat flux	$\dot{q}$	$\mathrm{W\,m^{-2}}$
Area-averaged absorber surface heat flux	$\dot{q}_{\mathrm{mean}}$	$\mathrm{W\,m^{-2}}$
Standard deviation of surface heat flux	$\sigma_{\dot{q}}$	$\mathrm{W\,m^{-2}}$
Absorber surface area	A	$\mathrm{m^2}$
Temperature uniformity factor	$\mathrm{UF_T}$	–
Local absorber surface temperature	T	K
Area-averaged absorber surface temperature	T_{mean}	K
Standard deviation of surface temperature	σ_T	K

Table 3: Heat Transfer and Flow Quantities

Quantity	Symbol	Unit
Reynolds number	Re	–
Prandtl number	Pr	–
Nusselt number	Nu	–
Useful thermal power absorbed by fluid	$\dot{Q}_{\mathrm{u}}$	W
Inner surface area of absorber tube	A_{i}	$\mathrm{m^2}$
Mean film temperature	T_{mf}	K
Bulk mean fluid temperature	T_{b}	K
Absorber pitch	p	m
Helix diameter	D	m
Outer diameter of absorber tube	d_{o}	m
Inner diameter of absorber tube	d_{i}	m
Non-dimensional pitch	p/d_{o}	–
Darcy friction factor	f	–
Dynamic viscosity at tube-wall temperature	μ_{w}	Pa s
Dynamic viscosity at bulk-fluid temperature	μ_{f}	Pa s